Co-cross-linking Silk Matrices with Silica Nanostructures for Robust Ultrathin Nanocomposites

Eugenia Kharlampieva,[†] Veronika Kozlovskaya,[†] Brett Wallet,[†] Valeriy V. Shevchenko,[‡] Rajesh R. Naik,[§] Richard Vaia,[§] David L. Kaplan,[⊥] and Vladimir V. Tsukruk[†],*

[†]School of Materials Science and Engineering, Georgia Institute of Technology, Atlanta, Georgia 30332, [‡]Institute of Macromolecular Chemistry, National Academy of Sciences of Ukraine, Kiev, Ukraine, [§]Air Force Research Laboratory, Materials and Manufacturing Directorate, Wright-Patterson AFB, Dayton, Ohio 45433, United States, and [⊥]Department of Biomedical Engineering, Tufts University, Medford, Massachusetts, 02155 United States

ABSTRACT   We report on a novel assembly approach to fabricate ultrathin robust freely standing nanocomposite membranes. The materials are composed of a pre-cross-linked silk fibroin matrix with incorporated silica nanoparticles with silsesquioxane cores (POSS) or clay nanoplatelets. These reinforced silk membranes have enhanced mechanical properties as compared to traditional silk-based nanocomposites reported previously. Up to 6-fold and 8-fold increase in elastic modulus and toughness, respectively, were found for these nanocomposites. In contrast, traditional LbL-assembled nanocomposites showed only a 3-fold increase in mechanical strength. The silk nanocomposites obtained also revealed excellent optical transparency in the visible region especially if reinforced with POSS nanoparticles, which suggests their utility as low cost, nontoxic, and easily scalable reinforced biomaterials for mechanically demanding applications.

KEYWORDS: silk nanocomposites · layer-by-layer · POSS · clay · mechanical properties

Bioenabled and bioderived nanocomposite materials have been designed and widely investigated as prospective advanced materials fabricated under environmentally benign conditions.[1,2] Biomaterials-based nanocomposites exhibit novel synergetic properties by integrating features from both bioderived and inorganic components and provide potential as biomedical materials and biomolecular devices.[3] These nanomaterials are prepared by the physical mixing of two components, *in situ* synthesis of inorganic nanostructures within organic matrixes, or by employing bottom-up approaches with step-by-step component assembly.[4,5] The latter strategy affords nanomaterials with enhanced interfacial strength because it overcomes problems with poorly controlled phase separation and allows precisely tailored composition, function, and tunable thickness, all at the nm-scale.

Silk fibroin has found growing interest as a key biomaterial component in hybrid nanocomposites with advanced performance.[6] Tissue engineering and biomedical applications are explored because of its biocompatibility and biodegradability.[7,8] Silk fibroin from silkworm cocoons can be processed as an aqueous solution which extends the range of silk materials from thin films to coatings and electrospun fibers.[9,10] Silk has excellent mechanical properties with high elastic modulus, elongation to break, and toughness.[11] However, silk-based membranes and films still lack mechanical robustness for demanding applications in biotechnology, and therefore an inorganic filler is frequently needed to reinforce silk-based nanocomposites. To date, reinforced silk-based bulk materials, films, and fibers have been obtained by utilizing inorganic nanofillers such as zirconia, silica, titania, apatite, or metal particles.[12,13]

Moreover, silk materials possess remarkable optical properties such as near-perfect transparency in a visible range.[14] In this respect, nanocomposites, consisting of transparent organic or polymeric matrices with embedded particles of diameters less than 50−100 nm, are finding increased attention in research on optical materials due to the low light intensity loss by scattering which is effectively reduced when compared to incorporated particles of larger dimensions.[15] The low light intensity loss is an important characteristic of these nanocomposites for optical applications such as nonlinear optics photoconductivity and as transparent UV-absorbing layers.[16]
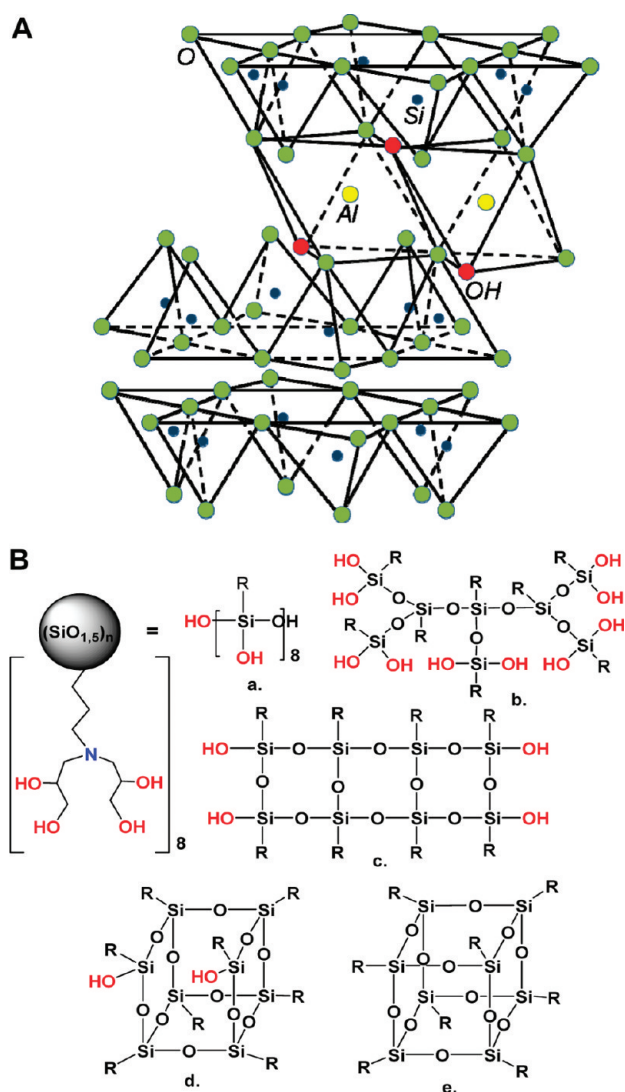
One of the most popular inorganic reinforcing components for polymer and natural nanocomposites is clay platelets (Figure 1) because of their outstanding mechanical values, high surface area, high aspect

A

B

Figure 1. Schematic presentation of MMT (A) and POSS structures (B). POSS is presented as a mixture of linear (a), branched (b), ladder-type (c), incompletely condensed polyhedral (d), and completely polyhedral structures (octahedral as an example, from ref 25) (e). The MMT structure A is redrawn from http://serc.carleton.edu/NAGTWorkshops/mineralogy/clay_mineralogy.html.

ratio, and compatibility with polymeric materials.[17,18] Incorporation of clay nanoparticles by either blending or by layer-by-layer (LbL) assembly resulted in clay–organic nanocomposites with significantly enhanced thermal and mechanical properties and reduced permeability.[19] We have recently shown that re-inforced silk–clay nanocomposite films can be obtained by spin-assisted LbL assembly of a silk fibroin matrix with clay (montmorillonite) (MMT) nanosheets.[20] The silk–clay nanocomposites exhibited significantly higher toughness and Young's modulus then those of pristine LbL silk membranes studied in our previous work. Conventional LbL assembly is based on alternating deposition of oppositely charged species and this approach has been applied to integrate synthetic and biological materials with inorganic moieties such as nanoparticles, nanosheets, and nanowires.[21] As known,

LbL assembly provides an opportunity to obtain well-defined and stratified films with tunable thickness, structure, and composition at the nanoscale level, which cannot be easily accomplished when casting solution mixtures or adding an inorganic component in the conventional LbL approach.[22]

Another promising candidate for multifunctional and lightweight nanocomposites is polyhedral oligomeric silsesquioxane (POSS), nanosized silica nanoparticles (Figure 1). Introduced as a new functionalized inorganic compound, POSS has attracted interest because of its facile preparation, low polydispersity, high transparency, high yield, and multiple functionalities. Moreover, POSS is inert, optically transparent, and stiff, with the Young's modulus reaching 7.5 GPa.[23] Moreover, it is a low cost and easily scalable material if a one-pot synthetic route is used to create modestly polydispersive POSS-M. The POSS-M material has several unique features: (1) the chemical composition is a hybrid, intermediate ($RSiO_{1.5}$) between that of silica (SiO_2) and silicone ($R2SiO$) and the (2) silica nanoparticles (2–4 nm) are comparable to common polymer dimensions and domains in silk materials.[24] Therefore, POSS has an organic–inorganic core structure, which provides rigidity while covalently bonded reactive functionalities make POSS compatible with interfaces.[25] As a result, the POSS compound has served as a reinforcing agent for polymer matrices, resulting in improved bulk thermal and mechanical properties.[26,27]

Despite significant progress in designing silk-based natural nanocomposites, many challenges remain in synthetic of natural multifunctional materials with well-organized structure, homogeneous composition, and distribution of nanofillers, and nanoscale control over film thickness especially for ultrathin (below 50 nm) films. Current attempts to fabricate silk-based nanocomposites usually result in brittle materials with compromised mechanical and optical properties. The ability to precisely construct silk-based architectures at the nanoscale will provide a means of producing biocompatible nanomaterials for advanced applications with requirements for miniaturization, light in weight, excellent toughness, and high flexibility.

In this study, we introduce a novel method for bottom-up fabrication of highly cross-linked silk-based nanocomposite membranes with significantly enhanced mechanical properties. The re-enforced nanomaterials were obtained by integrating silsesquioxane nanoscale cores (POSS-M) and MMT nanoplatelets with silk matrices which were premixed with glutaraldehyde (GA) as a cross-linking agent to increase matrix and interfacial strength. To achieve this goal, we introduced a novel one-step fabrication approach which involved step-by-step spin-assisted deposition of the three-component mixture of silk, cross-linking agent, and a nanofiller, and compared the results with conventional

spin-assisted LbL assembly which is usually employed for the fabrication of laminated nanocomposites.

The combination of conventional LbL assembly a with one-step mixed solution route could provide a unique opportunity to overcome major obstacles for developing high-performance silk-based nanocomposites. Premixing of components combined with silk cross-linking affords improved solubility and compatibility of the silk and inorganic materials and, therefore, a more homogeneous materials deposition in a single step. The latter issue is a significant challenge in traditional LbL assembly with alternating deposition of silk and inorganic nanostructures.[20] At the same time, the one-step one-solution approach holds advantages over the traditional LbL such as a nanoscale control over deposition into hierarchical structures and scaling up to higher film thicknesses. Thus, in contrast to previous studies on organic−inorganic composites fabricated by conventional LbL assembly or bulk mixing, the integration of approaches suggested in the present work might afford a higher degree of materials uniformity and enhanced physical properties critical for designing ultrathin (tens of a nanometer) biocompatible nanocomposites with advanced mechanical properties for potential applications as biosensors, as selective membranes, and in biomedical science.

RESULTS AND DISCUSSION

Nanocomposite Assembly. MMT clay exploited in this study belongs to the class of 2:1 phyllosilicates, nominally one-dimensional crystals comprising covalently bonded, aluminosilicate layers, ~0.96 nm thick and separated by a van der Waal interlayer, gallery containing charge-compensating alkali metal or earth cations (Figure 1a).[28] The charge per unit cell (generally between 0.5 and 1.3 for swellable smectites) originates from isomorphous substitution within the aluminosilicate layer (*e.g.*, tetrahedral Si^{4+} by Al^{3+} or octahedral Al^{3+} by Mg^{2+}). The number of exchangeable interlayer cations, the cation exchange capacity (CEC), generally ranges between 60 and 140 mequiv/100 g. Cloisite Na has a nominal unit cell formula of $Na_{0.66}[Si_{7.8}Al_{0.2}O_{16}][Al_{2.96}Fe_{0.45}Mg_{0.44}Ca_{0.02}O_4(OH)_4]$ and a CEC of 95 mequiv/100 g.[28]

POSS used in the study has different compositions of hydroxyl and tert-amine groups at their peripherals as illustrated in Figure 1b. POSS has an empirical formula of $[RSiO_{1.5}]_n$ (where $n = $ ~14 and R represents organic functional group $CH_2CH_2CH_2N[CH_2CH(OH)-CH_2OH]_2$) and is composed of a mixture of linear, branched, ladder-type, completely polyhedra, and incompletely condensed polyhedra structures. Nanoparticles are very uniform in size and have average dimensions of 2.5 nm.[25] Moreover, each POSS molecule contains a reactive organic shell for solubility and compatibility of the POSS segments with the various matrices.
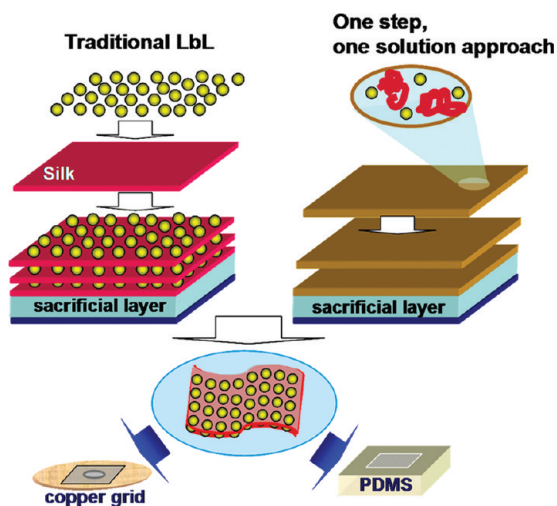

Figure 2. Two LbL approaches for the fabrication of reinforced silk nanocomposites: traditional LbL assembly (left) and one-step, one-solution LbL approach (right).

We found that traditional LbL assembly of silk and POSS resulted in linearly grown (silk−POSS)$_n$ nanocomposite films with a bilayer thickness of 4.2 nm (Figure 3). The result correlates well with the bilayer thickness for silk−MMT films.[20] Further exposure of the (silk−POSS)$_n$ and (silk−MMT)$_n$ matrices to glutaraldehyde (GA) solutions resulted in no change in film thicknesses.

In contrast to the traditional method of LbL deposition of different components, the one-step approach involved premixing silk and GA solutions followed by adding nanofiller dispersions (Figure 2). Indeed, both three-component films of (silk + GA + POSS) and (silk + GA + MMT) showed linear growth, indicating persistent and robust assemblies, similar to the two-component silk−POSS and silk−MMT systems. However, the (silk + GA + MMT) system possessed an increment 5.35 nm per layer which is thicker than that for a (silk−MMT) film of 4.1 nm/bilayer. The (silk + GA + MMT) nanocomposites exhibited similar linear growth with the layer thickness of 4.7 nm. The control experiment with a (silk + GA) film demon-
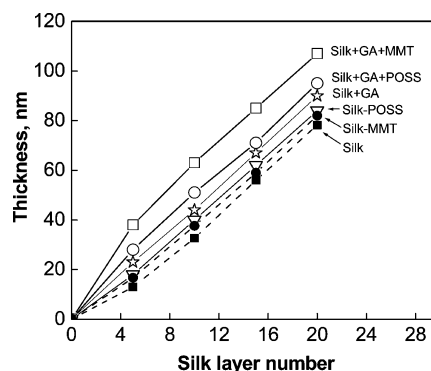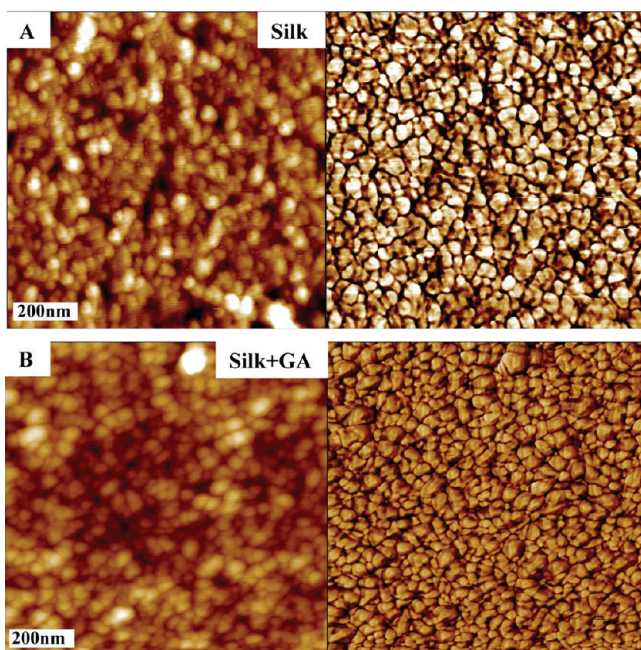

Figure 3. An increase in thickness of different silk LbL films with increasing numbers of deposited layers as measured by ellipsometry.

Figure 4. AFM topographical (left) and phase images (right) of silk surfaces with silk layers deposited from solution without cross-linking (A) and pre-cross-linked in solution before deposition (B). Height is 10 nm and z-scale is 20° (B).

strated that films of pre-cross-linked silk were thicker than those for the non-cross-linked one-component (silk) films showing layer thicknesses of 4.5 and 3.9 nm, respectively (Figure 3).

Surface Morphology. Figure 4 presents atomic force microscopy (AFM) topographical images of a single-layer silk film and a (silk + GA) film deposited from un-cross-linked and pre-cross-linked silk, respectively. AFM analysis of the images showed that both films have
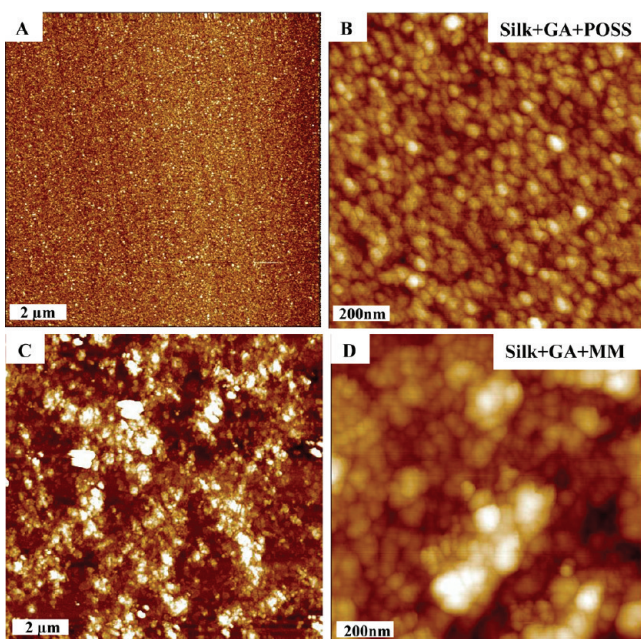
Figure 5. AFM topographical images of a single layer deposited from (silk + GA + POSS) (A, B) and (silk + GA + MMT) solutions (C, D). Heights are 10 nm (A, B), 40 nm (C), and 30 nm (D).

light-grainy morphology with a surface micro-roughness (rms) of 1.3 ± 0.2 nm and 1.2 ± 0.2 nm (within 1 × 1 μm² surface area) for the silk and (silk + GA) films, respectively. The surfaces were relatively smooth which is indicative of silk deposited from aqueous solutions on hydrophilic surfaces.[52,29] Slightly increased microroughness of ultrathin silk films (usually below 1 nm) can be attributed to grainy and nano-porous morphology caused by localized polymerization of silk chains similarly to that observed for highly cross-linked ultrathin polymer and aminoacid films as observed in our recent studies.[30]

On the other hand, the difference in thickness for the silk and (silk + GA) films revealed that GA provides some changes in the silk secondary structure which promoted thicker film formation (Figure 3). The GA-induced structural changes will be discussed later in this manuscript. However surface morphology of the three-component (silk + GA + POSS), obtained by adding POSS into a pre-cross-linked silk solution, remained similar to that observed for the pristine silk film with a similar microroughness of 1.1 ± 0.2 nm (Figure 5a,b). In contrast, incorporation of clay into a solution mixture resulted in more heterogeneous and much rougher and more porous surface films with a microroughness of 3.9 ± 0.2 nm (Figure 5c,d).

The difference in surface morphology in (silk + GA + POSS) and (silk + GA + MMT) systems can be attributed to the difference in nanofiller nature. Apparently, 2-nm POSS nanoparticles can be finely mixed with the silk amorphous phase and thus do not significantly affect surface morphology of silk with typical dimensions of the amorphous phase of 10−30 nm.[11] In contrast, clay nanoplatelets are highly polydisperse and have irregular sheetlike structures which are ∼1 nm thick and up to 200 nm wide.[20,28] Despite that the clay nanoplatelets are well-dispersed and do not form large microscopic aggregates in solution, they are not ideally oriented on a surface in a (silk + GA + MMT) film, leading to the high surface microroughness. This random structure is in contrast to the almost ideal planar orientation of clay nanoplatelets observed in a conventional LbL assembly of clay and silk.[20] Overall, the smoother (silk + GA + POSS) films are thinner in contrast to the (silk + GA + MMT) films.

Silk Structural Conformations Followed by ATR-FTIR. To further investigate the mechanism of cross-linking-induced enhancement of mechanical properties, silk fibroin was adsorbed on a silicon surface in a liquid cell followed by introducing the GA cross-linking agent into the liquid cell. The attenuated total reflection-Fourier-transform IR spectroscopy (ATR-FTIR) spectrum in Figure 6 shows that the silk has a random-coil conformation with the major peak centered at 1644 cm^{-1}, which correlates well with our previous results on a hydrogenated silk layer adsorbed on surfaces.[52] However, a drastic difference in the spectrum was observed
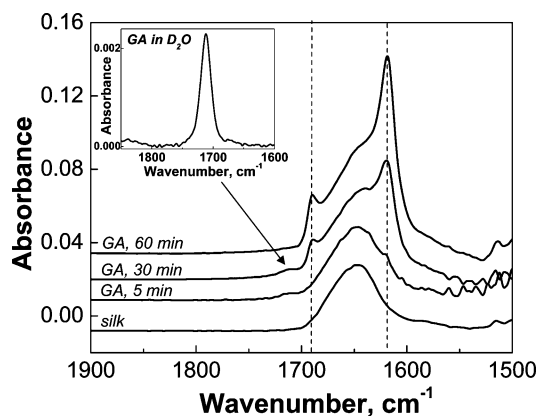
Figure 6. *In-situ* ATR-FTIR spectra of a silk layer before cross-linking (bottom spectrum) and after exposure to GA for different amounts of time. Silk was deposited *in situ* in a liquid cell from D_2O solutions on a Ge ATR crystal. Inset shows a GA spectrum in a D_2O solution.

in the presence of GA. Cross-linking resulted in a gradual decrease in random-coil silk I content (band at 1645 cm^{-1}) with an appearance of two peaks at 1688 and 1623 cm^{-1} attributed to significant presence of crystalline ss-sheets of silk II.[31,32] The transition is time-dependent with silk II features appearing in the spectrum in 5 min until the final transformation was completed in 60 min (Figure 6). In contrast, the hydrogenated silk layer retained its random-coil conformation for at least 4 days in the absence of GA.

Mechanical Properties. A typical buckling instability pattern under compressive stress illustrates that the film is uniform with periodic and equally spaced wrinkles, which can be exploited for the calculation of the compressive elastic modulus (Figure 7a). Figure 7 panels b and c also show the representative interference patterns of the silk−nanocomposite films under various pressures and stress−strain curves from bulging experiments, which enables the determination of the tensile mechanical properties.[10,49] It was shown that mechanical values increased with increase in film thickness until reaching a plateau.[19,48] In our previous work on thin silk nanocomposites (<100 nm in thickness), the plateau was reached at 50−60 nm.[20] On that basis, in our current study films of comparable thickness with the average range of 80 ± 10 nm are taken for the mechanical testing and presented in Tables 1 and 2.

As clear from this data, a significant enhancement of the mechanical properties is observed. First, it is worth noting that additional cross-linking of the (silk−MMT)$_{20}$ films with GA leads to minor changes in mechanical properties with a 15% increase in Young's modulus (Table 1). In contrast, (silk + GA + MMT)$_{15}$ films showed a 6-fold, improved Young's modulus, reaching 25 ± 2 GPa (Table 2). Correspondingly, the toughness for the films increased 3.5 times to 700 ± 80 kJ m^{-3}.

Moreover, a drastic, 8-fold increase in toughness was achieved for ((silk + GA)−MMT)$_{15}$ systems obtained by sequential assembly of (silk + GA) solution with clay particles which afforded 1600 ± 100 kJ m^{-3} (Table 2). We also found that even in the nanofiller-free (silk + GA)$_{20}$ films, obtained by assembly of silk premixed with GA, mechanical properties improved with almost a 2-fold increase in the elastic modulus and 3-fold increase in toughness. These results are in contrast to those for the (silk)$_{20}$ films exposed to GA after the film fabrication which showed no significant effect of the cross-linking on mechanical properties indicating modest diffusion of the cross-linking agent into silk matrix (Table 1). It is worth noting that in our previous work a (silk−MMT)$_{17}$ film exhibited a 3-fold increase in elastic modulus to 12 ± 2 GPa and a 4-fold increase in toughness to 950 ± 100 kJ m^{-3}.[20] Therefore, overall, by applying new silk processing, a 2-fold increase in both mechanical strength and toughness has been achieved in this study.

A similar trend was observed for POSS-containing silk nanocomposites. Incorporation of POSS by conven-

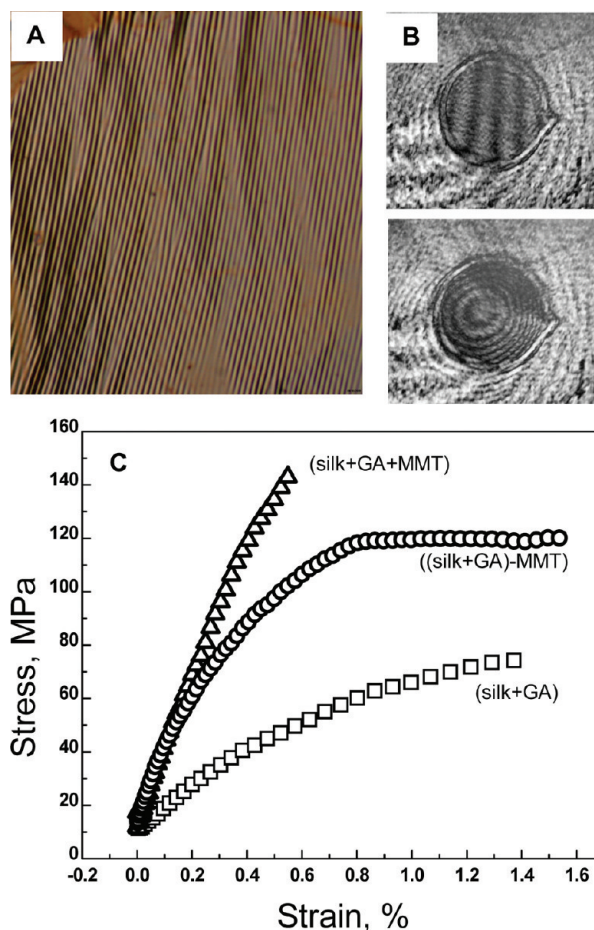**Figure 7.** Optical image of a compressed (silk + GA + POSS)$_{20}$ film during buckling measurements (A). An interference pattern of the (silk + GA + POSS)$_{20}$ film suspended over a 150 μm opening under 0 Pa (top) and 3000 Pa (bottom) in a bulging experiment (B). Stress−strain data for the silk containing pre-cross-linked films (C).

TABLE 1. Mechanical Properties of Silk Nanocomposite Films Prepared by the Traditional LbL Assembly[a]

silk and clay composites	film thickness (nm)	bulging Young's modulus (GPa)	buckling Young's modulus (GPa)	toughness (KJ m^{-3})
silk$_{20}$	80 ± 1.5	4.1 ± 1.0	3.2 ± 1.5	200 ± 50
(silk)$_{20}$, GA*	80 ± 2	5.0 ± 1.0	4.5 ± 1.5	250 ± 50
(silk−MMT)$_{20}$,	85 ± 1.5	12 ± 2.0	10.7 ± 1.5	950 ± 100
(silk−MMT)$_{20}$, GA*	85 ± 2.0	14 ± 2.0	12.1 ± 1.0	800 ± 100
(silk−POSS)$_{20}$	83 ± 1.5	10.3 ± 1.5	8.9 ± 1.5	850 ± 50

[a]GA* = films exposed to GA solutions after assembly.

tional LbL assembly with silk resulted in a significant enhancement of mechanical properties for (silk−POSS)$_{20}$ as indicated by a 2-fold increase in Young's modulus and 4-fold increase in toughness to 10.3 ± 1.5 GPa and 850 ± 50 kJ m^{-3}, respectively (Table 1). An alternative assembly of the premixed (silk + POSS) solutions lead to further increased elastic modulus up to 12 ± 1.5 GPa (Table 2). Further exposure of the (silk−POSS)$_{20}$ or (silk + POSS)$_{20}$ systems to the cross-linking solution did not affect mechanical values of the films (data not shown). In contrast, the drastic increase in mechanical properties was observed for the cross-linked blend (silk + GA + POSS)$_{20}$ systems which showed elastic modulus and toughness of 18 ± 1.5 GPa and 1000 ± 100 kJ m^{-3}, respectively (Table 2).

Finally, the effect of nanofiller volume fraction on composite performance was tested by varying the concentration of POSS solutions. The optimum concentration of POSS solution used to fabricate (silk−POSS) and (silk + POSS) films was found to be 0.2%. Up to this point, mechanical strength was in direct correlation with concentration, but a further increase in concentration to 1% resulted in brittle films. For example, 0.05% POSS solution afforded a 2-fold increase of both elastic modulus and toughness for (silk−POSS)$_{20}$ films, as compared to the pristine silk films (data not shown). The results on nanofiller concentration correlate well with those previously observed for (silk−MMT) composites.[20]

Optical Properties. Transparency of silk-based nanocomposite films was measured in a wavelength range between 190 and 800 nm (Figure 8). Both POSS- and MMT-containing nanocomposites were highly transparent in the visible region (400−800 nm) with a slight decrease at 228[9] and 260 nm[33] as a result of clay and silk absorbances, respectively. However, the transparency

in the UV region (190−350 nm) consistently decreased for (silk + GA + POSS) and (silk + GA + MMT) systems. The more pronounced loss in (silk + GA + MMT) transparency can be attributed to the higher scattering of the films when compared to the highly transparent (95%) conventional silk−MMT films observed earlier.[20] As supported by the AFM results, the surface microroughness of (silk + GA + MMT) nanocomposites was higher than that for the (silk + GA + POSS) materials because of the large dimensions and random orientation of clay platelets at the interface.

The refractive index and absorption coefficients for the silk and silk composites are shown in Figure 9. The refractive indices for the silk, silk−POSS, and silk−MMT samples, at a wavelength of 543 nm, are unexpectedly low, being 1.23, 1.29, and 1.37, respectively (Figure 9a). The measured thicknesses of the samples were 22.8, 32.8, and 74.8 nm for silk, (silk + GA + POSS), and (silk + GA + MMT), respectively. The results designate that both POSS and MMT nanofillers induced an increase in the refractive index. The data correlate well with the previously reported increases in the refractive index of a material with increasing density and cross-linking of nanofillers within thin films.[34] The fact that the silk−MMT sample represents the highest value suggests that the MMT platelets contribute more in composite refractive index than very fine POSS nanoparticles, which correlates well with the optical density data.[35]

The refractive index value for the silk films are much lower than previous results for the refractive index of silk fibers, $n = 1.538$.[36] Another study determined the refractive index of silk fibroin filament to be 1.34.[37] The differences may be within the aqueous processing approach used for the films, compared to silk fibers in their native form. However, the most probable cause is

TABLE 2. Mechanical Properties of Silk Nanocomposite Films Prepared by Utilizing the One-Step, One-Solution Approach

| silk and clay composites	film thickness (nm)	bulging Young's modulus (GPa)	buckling Young's modulus (GPa)	toughness (KJ m^{-3})
(silk + GA)$_{20}$,	90 ± 1.5	6.8 ± 2.0	5.7 ± 0.5	700 ± 80
(silk + GA + MMT)$_{15}$	80 ± 1.5	25 ± 2.0	21 ± 1.5	700 ± 100
((silk + GA)−MMT)$_{15}$	72 ± 1.2	20 ± 2.0	16.8 ± 2.0	1600 ± 150
(silk + POSS)$_{20}$	86 ± 1.5	12 ± 1.5	10 ± 1.5	800 ± 50
(silk + GA + POSS)$_{20}$	95 ± 1.5	18 ± 2.0	15.4 ± 1.5	1000 ± 100
((silk + GA)−POSS)$_{15}$	71 ± 1.5	10 ± 2.0	7 ± 1.5	1420 ± 150
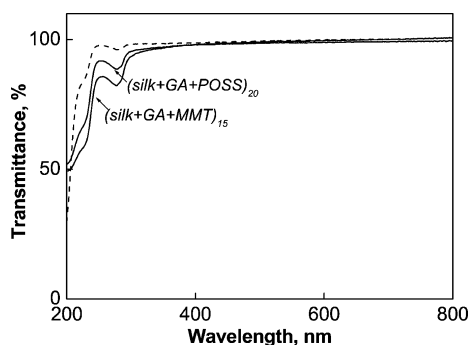
Figure 8. Transmission of (silk + GA + MMT)$_{15}$ and (silk + GA + POSS)$_{20}$ films. Transmission of a pristine (silk)$_{20}$ film is presented as a dashed line. Data for a quartz substrate was taken as a background.

highly grainy surface morphology and developed porosity of highly cross-linked silk matrices with nanometer thickness in contrast to that of silk films obtained *via* conventional spin-casting with uniform surface morphology.[10] The excessive porosity at nanoscale does not bring excessive light scattering but reduces effective refractive power of polymer films. Considering that the highest porosity should concentrate along the substrate−film and air−film interfaces due to excessive interfacial stresses, one should expect this effect to be much more pronounced for smaller film thicknesses and diminished for thicker films. To test this suggestion, we fabricated a set of multilayered silk films with an increasing thickness up to 85 nm (Figure 9b). For these pure silk films with increasing thickness we indeed observed a gradual increase in an overall level of the refractive index without significant changes of the wavelength variation. For the thickest silk films tested here, which started reaching regular "bulk" state, we observed refractive index values approaching 1.52, a common value for dense bulk silks.[36] This trend indicates that decreasing interfacial porosity brings the refractive properties in line with expected bulk values.

The absorption coefficients were found to be around 0.03, 0.04, and 0.13 for the silk, (silk + GA + POSS), and (silk + GA + POSS) samples, respectively (Figure 9c). The values were relatively low indicating that the films exhibited low optical absorption and were relatively transparent, confirming the aforementioned conclusion. The trend observed for the absorption coefficient, k, reveals that both types of nanofillers increased the amount of light scattering for the silk films, indicating that an increase in density of the silk-films occurred after nanofiller inclusion. However, the use of fine silica POSS nanoparticles resulted in a much lower value for k, comparable to the original silk matrices.

General Discussion and Conclusion. The data provided here indicate that the one-step, one-solution fabrication LbL route with inclusion of silk matrix cross-linking
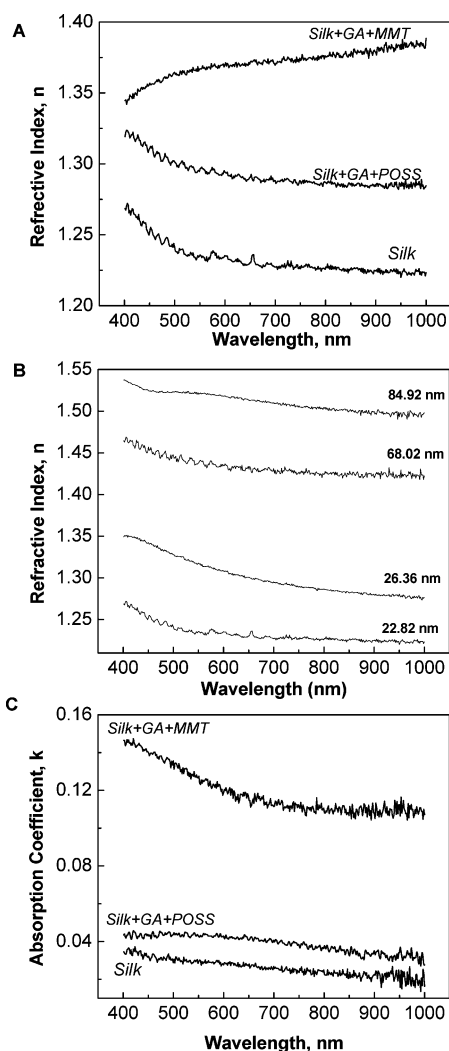
Figure 9. Refractive indices (a, b) and absorption coefficients (c) obtained for silk, (silk + GA+POSS), and (silk + GA + MMT) films. Thickness of silk films was of 22.82, 26.36 nm, 68.02 nm, and 84.92 nm as measured by ellipsometry (B).

appears to be more efficient for obtaining reinforced nanocomposite films with enhanced mechanical properties than the traditional LbL assembly route explored in earlier studies. Both methods allowed for the introduction of nanofillers which significantly improved mechanical properties; however, the one-step mixed-solution approach afforded an additional 2-fold increase in mechanical strength due to the concurrent cross-linking. The highest elastic moduli were observed for (silk + GA + MMT) films, which showed 6-fold and 5-fold enhancements, respectively, when compared to the pristine silk matrix, reaching a remarkable 25 GPa for elastic modulus, 1.6 MJ/m^3 for toughness, and 150 MPa for ultimate strength.

In situ ATR-FTIR revealed that the GA cross-linker reacted successfully with amorphous silk solutions inducing gradual silk crystallization. It has been previously reported that silk fibroin undergoes structural transitions from random-coil silk I into crystalline silk II as a result of dehydration induced by a treatment with organic sol-

vents, elevated temperatures, or by simple drying.[38] Our results indicate that such transformations can also be induced by covalent cross-linking as well. Indeed, silk has hydroxyl and amino groups such as serine, lysine, and arginine capable of chemical reactions with the GA cross-linking agent.[6,52] The results on silk conformational changes correlate well with the previously published data on cross-linking silk—chitosan blends with genipin, which also induced formation of β-sheet structures in initially amorphous silk.[39] In the latter case, ester groups of genipin interact with the amino groups of chitosan and silk, which leads to the formation of secondary amide linkages. In our case the change in the silk secondary structure provides an increase in film thickness observed in Figure 3. Indeed, β-sheet-rich silk is more hydrophobic than random silk and promotes thicker films when deposited on a surface. Moreover, silk transformation into a partially crystalline structure is responsible for the improved mechanical properties of the films.

In contrast, the silk-based nanocomposite films assembled by the traditional route cannot be further reinforced by exposure to the cross-linking agent. The results are in contrast to the previously observed cross-linking of LbL polyelectrolyte films with incorporated MMT particles.[40] In that case, GA was utilized to covalently cross-link hydroxyl groups of MMT and poly(vinyl alcohol) in the preassembled polyelectrolyte—MMT matrices, which significantly improved mechanical properties.[40] We suggest that in our case exposure to GA results in no significant enhancement in the preassembled silk films, because of limited diffusion of GA into the bulk silk. Indeed, dried silk is partially crystalline and adopts an ss-sheet-rich structure (silk II) when assembled by spin-assisted LbL, as a result of chain dehydration during spinning.[52] In contrast, when silk is in the random coil form and soluble in aqueous solutions the functional groups are easily accessible for the cross-linker, and efficient covalent cross-linking occurs in mixed solution. Moreover, the solution of partially cross-linked silk is clear, which favors stable aqueous dispersions with uniformly distributed components.

Comparison of nanocomposites with POSS *vs* MMT reinforcing agents shows that (silk + GA + POSS) films revealed slightly lower mechanical properties than (silk + GA + MMT) nanocomposite films: the elastic modulus reaches 18 GPa and toughness is 1.4 MJ/m³. Considering that POSS nanoparticles are comparable with dimensions of the silk random-coils (5—10 nm) structure, we can expect a significant affect on mechanical properties.[11] Moreover, the recent theoretical studies on the dimensions of crystalline domains in silk fibroin showed the nanocrystals to be of 1—2 and 2—3 nm in length and height, respectively.[41] This means that the nanocrystals, which are responsible for the strength characteristics of silk and formed by either hydrogen-bonded β-sheets as physical cross-links or by chemical cross-linking, have dimensions similar to those of POSS nanoparticles, thus reducing the entropic barrier for mixing with the silk matrix. The observation that the Young's modulus in the case of POSS-containing films was still lower than that for those with MMT can be explained by the initially lower elastic modulus of POSS itself (7.5 GPa) as compared to that of the clay (270 GPa), thus reducing the overall reinforcing effect. Both nanocomposites showed high stability upon degradation for at least 10 months. Further investigation of a long-time failure mechanism would be interesting to perform in the future.

Optical properties were also affected by nanofiller incorporation. The inclusion of nanofillers did not compromise transparency of the films in the visible region, the refractive index of MMT—silk nanocomposites was higher than that for the POSS systems. This relationship correlates well with the ellipsometric results on the absorption coefficients showing that the MMT-containing film scatters more light (higher k) than the POSS-containing samples. Furthermore, much smaller POSS nanoparticles uniformly distributed in the silk matrix more efficiently reduce overall fluctuations of the refractive index between the less-ordered phase and β-crystalline domains thus resulting in minimized optical losses in POSS-silk nanocomposites. This combination of enhanced mechanical and good optical properties suggests the perspective use of the silk-based nanocomposites as mechanically robust materials with optical transparency requirements.

In summary, ultrathin novel nanocomposite membranes with remarkable mechanical properties were generated by using a single-solution approach. In contrast to traditional LbL, the approach introduced here is (1) simpler, (2) more efficient, and (3) affords the assembly of homogeneous dispersions resulting in significantly re-enforced composites. The re-enforced nanomaterials were obtained by integrating POSS nanoparticles and MMT nanoplatelets with silk matrices which were premixed with a cross-linking agent. We found that covalent cross-linking induced silk crystallization into β-sheet domains, the effect previously found for dehydrated silk films as a result of formation of physical cross-links between neighboring silk segments. A computational analysis of the reinforcing phenomena, applied recently by Buehler *et al.* to the spider silk crystallization, could be one of the future directions for the current work.[42]

The attractive characteristics of these silk—inorganic nanocomposites include transparency, the use of low cost and nontoxic raw materials, and easy scale-up. The properties of the composites are attributed to the strong inter- and intramolecular interactions induced by physical and chemical cross-linking resulting in crystallization; and to the excellent dispersion of nanofiller particles

in the silk matrix. The facile and simplified fabrication method with the pre-cross-linked silk matrix described here can be further tailored by applying different conditions and the incorporation of inorganic species of various functionalities into silk matrix to obtain thin films with unique properties.

EXPERIMENTAL SECTION

Materials. A silk-fibroin solution was prepared from *Bombyx mori* silkworm cocoons as described previously.[43] Briefly, cocoons were boiled for 30 min in an aqueous solution of 0.02 M Na_2CO_3 of sodium carbonate for 45 min to extract sericin, rinsed thoroughly with distilled water, and dried. The dry fibroin bundle was then dissolved in a 9.3 M aqueous solution of lithium bromide at 60 °C for 4 h and dialyzed against distilled water at room temperature for 3 days to remove the salt. The resulting solution was extracted from the dialysis cassettes (Slide-a-Lyzer, Pierce, molecular weight cutoff (MWCO) 3500) and remaining particulates were removed through centrifugation and syringe-based microfiltration (5 mm pore size, Millipore). This process enables the production of 8−10% w/v silk fibroin solution which was dissolved with Nanopure water to a 0.2% solution and used for LbL assembly. Nanopure water with a resistivity of 18.2 MΩ cm was used in all experiments.

Montmorillonite (MMT, Cloisite Na) was supplied in powder form by Southern MMT Products (Figure 1). POSS-M, denoted as POSS in the manuscript, refers to mixed silsesquioxane cores (polyhedra, incompletely condensed polyhedra, ladder-type structures, linear structures, and all the possible combinations), in contrast to the geometrically specific POSS compounds (Figure 1). The POSS cores were synthesized by hydrolytic condensation of the precursor on a base of 3-aminopropyl triethoxysilane with a 2-fold molar excess of glycidol according to a well-established procedure.[44] Glutaraldehyde (70% in H_2O, Aldrich) was diluted to 2% solution with water.

Instrumentation. AFM images were collected in the tapping mode with silicon tips with a spring constant of 50 N/m on a Dimension 3000 AFM microscope (Digital Instruments) according to usual procedure.[45] Transmittance spectra of the composite films were obtained on quartz substrates using a UV-2450 spectrophotometer (Shimadzu).

Ellipsometry was utilized to determine both the thickness and optical properties of the silk-nanocomposite films. A Woollam M2000U variable-angle spectroscopic ellipsometer system was used, and the reflected polarization states were acquired over the range 400−1000 nm at 1.59-nm intervals and at angles of incidence equal to 65°, 70°, and 75°. All data analyses were performed using Windows version WVASE32 software. The dispersion in the refractive index was modeled using a Cauchy fit and determined from the polarization data of the thin film samples and derived refractive indices. The complex refractive index is given by the equation ($n = n + ik$), where n is associated with the real part and corresponds to the refractivity of the material.[46] The ik is the imaginary part and corresponds to the light absorption of the material. The absorption coefficient, k, is a measure of the light scattering within a medium and absorption, with low values designating high optical transparency.

Buckling. Buckling tests were conducted to evaluate the compressive elastic modulus of composite membranes from the elastic buckling instability.[10] Buckling was achieved by the compression of the films deposited on PDMS substrate in accordance with a prior approach.[47] This method uses the strain-induced elastic buckling instability and can be applied to thin films.[48] For an isotropic thin membrane, a uniform buckling pattern with a characteristic wavelength, k, is observed when it is subjected to a critical compressive stress.[49] The spacing of this pattern is directly related to the elastic modulus. To initiate the buckling pattern, a 2 mm × 2 mm membrane piece was placed over a 0.6 cm × 0.6 cm × 0.4 cm PDMS substrate, which was slowly compressed with micrometer-sized increments. The compression was monitored in differential interference contrast (DIC) mode adjusted for maximum contrast. Optical images were captured with a Leica MZ16 microscope in reflection mode.

Bulging Test. Bulging tests were performed using a custom-made interferometer equipped with a charge coupled device (CCD) camera (Logitech) and a He−Ne laser (k = 632.8 nm). Pressures up to 5000 Pa were exerted using a 60 mL syringe regulated by an automatic pump (Kent Scientific, Inc.) and monitored with an automatic pressure gauge, DPM 0.1 (SI Pressure Instruments). The bulging test data were analyzed using a model for the elastic deformation of circular membranes, according to procedures described previously.[50] The LbL membranes freely suspended over a copper substrate with a 150-μm hole were first inspected under an optical microscope, and a minimal pressure was exerted to check for symmetrical Newton's ring patterns that indicate membrane homogeneity before full load.

Construction of Nanocomposite Films. Figure 2 demonstrates two main fabrication approaches utilized in the study. In the first route, silk composites were obtained by traditional LbL assembly from silk and nanofiller solutions. The method represents a traditional two-step approach which utilizes two different solutions in an alternating manner as previously applied to the systems of synthetic polyelectrolytes and clay nanosheets. First, multilayer silk and composite films were produced through deposition by the spin-assisted LbL (SA-LbL) method as described elsewhere (Figure 2).[10] The depositions were performed either by the traditional alternating layers of silk and nanofiller particles (POSS or MMT)[6,51] or by using a one-step, single solution approach. For the traditional LbL assembly, 30 μL of 0.2% silk aqueous solutions and nanofiller dispersion were sequentially dropped on silicon substrates precoated with sacrificial acetate cellulose and rotated for 20 s with a 3000-rpm rotation speed, rinsing twice with Nanopure water between the deposition steps. Thus, n-bilayer silk−MMT or silk−POSS films denoted as (silk−MMT)$_n$, or (silk−POSS)$_n$, respectively, were constructed. To perform cross-linking with different densities of cross-linking, the films were exposed to GA for 2, 5, 10, or 20 h.

In the one-step assembling approach, a mixed, three-component (silk, nanofiller, and GA) solution was sequentially deposited on a silicon substrate (Figure 2). The final concentrations of silk, nanofiller, and GA in the solution mixture were 0.5%, 0.2%, and 2%, respectively. The films were denoted as (silk + GA + MMT)$_n$, or (silk + GA + POSS)$_n$.

***In Situ* ATR-FTIR.** Silk deposition and cross-linking were monitored by infrared spectroscopy using ATR-FTIR.[52] A Bruker FTIR spectrometer (Vertex 70) was equipped with a narrow-band mercury cadmium telluride detector. The internal compartment of the FTIR spectrometer containing the liquid cell was purged with dry nitrogen. The ATR surface was rectangular trapezoidal multiple reflection of a Ge crystal of dimension 50 mm × 10 mm × 2 mm (Harrick Scientific) whose beam entrance and exit surfaces were cut at 45 deg. Interferograms were collected at 4 cm^{-1} resolution, and the number of averaged scans was 120. Each interferogram was corrected on the corresponding background, measured for the same ATR cell with the same D_2O. To eliminate overlap of the IR bands in the 1700−1500 cm^{-1} region with the strong water band, D_2O with 99.9% isotope content was utilized.

For silk deposition *in situ*, 0.2% silk solutions in D_2O were adsorbed onto the surface of an oxidized Ge crystal for 10 min within the custom-made flow-through ATR-FTIR liquid cell (Harrick Scientific). After silk adsorption the silk solution was replaced with pure D_2O. Use of multiple-reflection ATR along with a flow-trough liquid cell allowed *in situ* deposition and compositional monitoring of ultrathin films (∼several nm in thickness).[52] Cross-linking was performed *in situ* by filling the cell with 2% GA in D_2O solution, keeping the crystal exposed to the solution for various amounts of time, followed by extensive rinsing with a pure D_2O solution. The individual spectrum of GA was obtained in D_2O solution by taking the clean crystal as background. It is worth noting that on the basis of our ATR results we allowed silk to be

REFERENCES AND NOTES

1. Brutchey, R. L.; Morse, D. E. Silicatein and the Translation of its Molecular Mechanism of Biosilicification into Low Temperature Nanomaterial Synthesis. *Chem. Rev.* **2008**, *108*, 4915–4934.

2. Dickerson, M. B.; Sandhage, K. H.; Naik, R. R. Protein- and Peptide-Directed Syntheses of Inorganic Materials. *Chem. Rev.* **2008**, *108*, 4935–4978.

3. Lewis, R. Spider Silk: Ancient Ideas for New Biomaterials. *Chem. Rev.* **2006**, *106*, 3762–3774.

4. Jiang, C.; Markutsya, S.; Shulha, H.; Tsukruk, V. V. Freely Suspended Gold Nanoparticles Arrays. *Adv. Mater.* **2005**, *17*, 1669–1673.

5. Kharlampieva, E.; Slocik, J. M.; Singamaneni, S.; Poulsen, N.; Kroger, N.; Naik, R. R.; Tsukruk, V. V. Protein-Enabled Synthesis of Monodisperse Titania Nanoparticles on and within Polyelectrolyte Matrices. *Adv. Funct. Mater.* **2009**, *19*, 2303–2311.

6. Porter, D.; Vollrath, F. Silk as a Biomimetic Ideal for Structural Polymers. *Adv. Mater.* **2009**, *21*, 487–492.

7. Li, C.; Kaplan, D. L. Biomimetic Composites *via* Molecular Scale Self-Assembly and Biomineralization. *Curr. Opin. Solid. State. Mater. Sci.* **2003**, *7*, 265–271.

8. Heim, M.; Keerl, D.; Scheibel, T. Spider Silk: From Soluble Protein to Extraordinary Fibers. *Angew. Chem.* **2009**, *48*, 2–15.

9. Nogueira, G. M.; Swiston, A. J.; Beppu, M. M.; Rubner, M. F. Layer-by-Layer Deposited Chitosan/Silk Fibroin Thin Films with Anisotropic Nanofiber Alignment. *Langmuir* **2010**, *26*, 8953–8958.

10. Jiang, C.; Wang, X.; Gunawidjaja, R.; Lin, Y.-H.; Gupta, M.; Kaplan, D. L.; Naik, R. R.; Tsukruk, V. V. Mechanical Properties of Robust Ultrathin Silk Fibroin Films. *Adv. Funct. Mater.* **2007**, *17*, 2229–2237.

11. Shulha, H.; Foo, C. W. P.; Kaplan, D. L.; Tsukruk, V. V. Unfolding the Multilength Scale Domain Structure of Silk Fibroin Protein. *Polymer* **2006**, *47*, 5821–5830.

12. Blond, D.; McCarthy, D. N.; Blau, W. J.; Coleman, J. N. Toughening of Artificial Silk by Incorporation of Carbon Nanotubes. *Biomacromolecules* **2007**, *8*, 3973–3976.

13. Lee, S.-M.; Pippel, E.; Göselle, U.; Dresbach, C.; Qin, Y.; Chandran, C. V.; Bruniger, T.; Hause, G.; Knez, M. Greatly Increased Toughness of Infiltrated Spider Silk. *Science* **2009**, *324*, 488–492.

14. Omenetto, F. G.; Kaplan, D. L. A New Route for Silk. *Nat. Photon.* **2008**, *2*, 641–643.

15. Caseri, W. Nanocomposites of Polymers and Metals or Semiconductors: Historical Background and Optical Properties. *Macromol. Rapid Commun.* **2000**, *21*, 705–722.

16. Kyprianidou-Leodidou, T.; Margraf, P.; Caseri, W.; Suter, U. W.; Walther, P. Polymer Sheets with a Thin Nanocomposite Layer Acting as a UV Filter. *Polym. Adv. Technol.* **1997**, *8*, 505–512.

17. Podsiadlo, P.; Michel, M.; Critchley, K.; Srivastava, S.; Qin, M.; Lee, J. W.; Verploegen, E.; Hart, A. J.; Qi, Y.; Kotov, N. A. Diffusional Self-Organization in Exponential Layer-by-Layer Films with Micro- and Nanoscale Periodicity. *Angew. Chem.* **2009**, *48*, 7073–7077.

18. Lvov, Y. M.; Shchukin, D. G.; Möhwald, H.; Price, R. R. Halloysite Clay Nanotubes for Controlled Release of Protective Agents. *ACS Nano* **2008**, *2*, 814–820.

19. Tang, Z.; Kotov, N. A.; Magonov, S.; Ozturk, B. Nanostructured Artificial Nacre. *Nat. Mater.* **2003**, *2*, 413–418.

20. Kharlampieva, E.; Kozlovskaya, V.; Gunawidjaia, R.; Shevchenko, V. V.; Kaplan, D.; Vaia, R.; Naik, R. R.; Tsukruk, V. V. Flexible Silk−Inorganic Nanocomposites: From Transparent to Highly Reflective. *Adv. Funct. Mater.* **2010**, *20*, 840–846.

21. Stuart, M. C.; Huck, W.; Genzer, J.; Müller, M.; Ober, C.; Stamm, M.; Sukhorukov, G.; Szleifer, I.; Tsukruk, V. V.; Urban, M.; Winnik, F.; Zauscher, S.; Luzinov, I.; Minko, S. Emerging Applications of Stimuli-Responsive Polymer Materials. *Nat. Mater.* **2010**, *9*, 101–113.

22. Lutkenhaus, J.; Hammond, P. Electrochemically Enabled Polyelectrolyte Multilayer Devices: From Fuel Cells to Sensors. *Soft Matter* **2007**, *3*, 804–816.

23. Pescarmona, P. P.; Maschmeyer, T. Oligomeric Silsesquioxanes: Synthesis, Characterization, and Selected Applications. *Aust. J. Chem.* **2001**, *54*, 583–596.

24. Wu, J.; Mather, P. T. POSS Polymers: Physical Properties and Biomaterials Applications. *J. Macromol. Sci. Part C* **2009**, *49*, 25–63.

25. Gunawidjaja, R.; Huang, F.; Gumenna, M.; Klimenko, N.; Nunnery, G. A.; Shevchenko, V.; Tannenbaum, R.; Tsukruk, V. V. Ordering and Behavior of Branched Amphiphilic Polyhedral Silsesquioxane POSS-M Compounds. *Langmuir* **2009**, *25*, 1196.

26. Carroll, J. B.; Waddon, A. J.; Nakade, H.; Rotello, V. M. "Plug and Play" Polymers. Thermal and X-ray Characterizations of Non-covalently-Grafted Polyhedral Oligomeric Silsesquioxane (POSS)−Polystyrene Nanocomposites. *Macromolecules* **2003**, *36*, 6289–6291.

27. Iacono, S. T.; Budy, S. M.; Mabry, J. M.; Smith, D. W., Jr. Synthesis, Characterization, and Surface Morphology of Pendant Polyhedral Oligomeric Silsesquioxane Perfluorocyclobutyl Aryl Ether Copolymers. *Macromolecules* **2007**, *40*, 9517–9522.

28. Drummy, L. F.; Koerner, H.; Farmer, K.; Tan, A.; Farmer, B. L.; Vaia, R. A. High-Resolution Electron Microscopy of Montmorillonite and Montmorillonite/Epoxy Nanocomposites. *J. Phys. Chem. B* **2005**, *109*, 17868–17878.

29. Gupta, M.; Singamaneni, S.; McConney, M.; Drummy, L. F.; Naik, R. R.; Tsukruk, V. V. A Facile Fabrication Strategy for Patterning Protein Chain Conformation in Silk Materials. *Adv. Mater.* **2010**, *22*, 115–119.

30. Anderson, K. D.; Marczewski, K.; Singamaneni, S.; Slocik, J. M.; Jakubiak, R.; Naik, R. R.; Bunning, T. J.; Tsukruk, V. V. Plasma Amino Acid Coatings for a Conformal Growth of Titania Nanoparticles. *ACS Appl. Mater. Interfaces* **2010**, *2*, 2269–2281.

31. Dicko, C.; Knight, D.; Kenney, J.; Vollrath, F. Secondary Structures and Conformational Changes in Flagelliform, Cylindrical, Major, and Minor Ampullate Silk Proteins. Temperature and Concentration Effects. *Biomacromolecules* **2004**, *5*, 2105–2115.

32. Hermanson, K.; Huemmerich, D.; Scheibel, T.; Bausch, A. R. Engineered Microcapsules Made of Reconstituted Spider Silk. *Adv. Mater.* **2007**, *19*, 1810–1815.

33. Beall, G. W.; Sowersby, D. S.; Roberts, R. D.; Robson, M. H.; Lewis, L. K. Analysis of Oligonucleotide DNA Binding and Sedimentation Properties of Montmorillonite Clay Using Ultraviolet Light Spectroscopy. *Biomacromolecules* **2009**, *10*, 105–112.

34. Anderson, K. D.; Slocik, J. M.; McConney, M. E.; Enlow, J. O.; Jakubiak, R.; Bunning, T. J.; Naik, R. R.; Tsukruk, V. V. Facile Plasma-Enhanced Deposition of Ultrathin Crosslinked Amino Acid Films for Conformal Biometallization. *Small* **2009**, *5*, 741–749.

35. Kopesky, E. T.; Haddad, T. S.; McKinley, G. H.; Cohen, R. E. Miscibility and Viscoelastic Properties of Acrylic Polyhedral Oligomeric Silsesquioxane−Poly(methyl methacrylate) Blends. *Polymer* **2005**, *46*, 4743–4752.

36. Lewin, M., Pearce, E. *Handbook of Fiber Chemistry*; Robson, R. M., Ed.; International Fiber Science and Technology Series, Vol. 15; Marcel Dekker, Inc.: New York, 1998; pp 415−456.

37. Tajima, F. Development of Measurement System for Diameter and Refractive Index of Silk Fibroin Filament Based on Scattered Light Pattern. *J. Insect Biotechnol. Sericol.* **2004**, *73*, 85–88.

38. Rousseau, M.-E.; Beaulieu, L.; Lefèvre, T.; Paradis, J.; Asakura, T.; Pèzolet, M. Characterization by Raman Microspectroscopy of the Strain-Induced Conformational Transition in Fibroin Fibers from the Silkworm *Samia Cynthia Ricini*. *Biomacromolecules* **2006**, *7*, 2512–2521.

39. Silva, S. S.; Motta, A.; Rodrigues, M. T.; Pinheiro, A. F. M.; Gomes, M. E.; Mano; Jo, F.; Reis, R. L.; Migliaresi, C. Novel Genipin-Cross-Linked Chitosan/Silk Fibroin Sponges for Cartilage Engineering Strategies. *Biomacromolecules* **2008**, *9*, 2764.

40. Podsiadlo, P.; Kaushik, A. K.; Arruda, E. M.; Waas, A. M.; Shim, B. S.; Xu, J.; Nandivada, H.; Pumplin, B. G.; Lahann, J.; Ramamoorthy, A.; Kotov, N. A. Ultrastrong and Stiff-Layered Polymer Nanocomposites. *Science* **2007**, *318*, 80–83.

41. Keten, S.; Xu, Z.; Ihle, B.; Buehler, M. J. Nanoconfinement Controls Stiffness, Strength, and Mechanical Toughness of Beta-Sheet Crystals in Silk. *Nat. Mater.* **2010**, *9*, 359–167.

42. Keten, S.; Buehler, M. J. Atomistic Model of the Spider Silk Nanostructure. *Appl. Phys. Lett.* **2010**, *96*, 153701–153703.

43. Sofia, S.; McCarthy, M. B.; Gronowicz, G.; Kaplan, D. L. Functionalized Silk-Based Biomaterials for Bone Formation. *J. Biomed. Mater. Res.* **2001**, *54*, 139–148.

44. Tereshchenko, T. A.; Shevchuk, A. V.; Shevchenko, V. V.; Snegir, S. V.; Pokrovskii, V. A. Alkoxysilyl Derivatives of Polyhedral Oligosilsesquioxanes Containing Amino and Hydroxyl Groups and Sol- Gel Hybrid Materials on their Basis. *Polym. Sci., Ser. A* **2006**, *48*, 1248–1256.

45. McConney, M. E.; Singamaneni, S.; Tsukruk, V. V. Probing Soft Matter with the Atomic Force Microscopies: Imaging and Force Spectroscopy. *Polym. Rev.* **2010**, *50*, 235–286.

46. Jiang, H.; Johnson, W. E.; Grant, J. T.; Eyink, K.; Johnson, E. M.; Tomlin, D. W.; Bunning, T. J. Plasma Polymerized Multilayered Photonic Films. *Chem. Mater.* **2003**, *15*, 340–347.

47. Stafford, C. M.; Harrison, C.; Beers, K. L.; Karim, A.; Amis, E. J.; Vanlandingham, M. R.; Kim, H. C.; Volksen, W.; Miller, R. D.; Simonyi, E. E. A Buckling- Based Metrology for Measuring the Elastic Moduli of Polymeric Thin Films. *Nat. Mater.* **2004**, *3*, 545–550.

48. Nolte, A. J.; Rubner, M. F.; Cohen, R. E. Determining the Young's Modulus of Polyelectrolyte Multilayer Films *via* Stress-Induced Mechanical Buckling Instabilities. *Macromolecules* **2005**, *38*, 5367–5370.

49. Jiang, C.; Singamaneni, S.; Merrick, E.; Tsukruk, V. V. Complex Buckling Instability Patterns of Nanomembranes with Encapsulated Gold Nanoparticle Arrays. *Nano Lett.* **2006**, *6*, 2254–2259.

50. Jiang, C.; Markutsya, S.; Pikus, Y.; Tsukruk, V. V. Freely Suspended Nanocomposite Membranes as Highly-Sensitive Sensors. *Nat. Mater.* **2004**, *3*, 721–728.

51. Hua, F.; Cui, T.; Lvov, Y. M. Ultrathin Cantilevers Based on Polymer−Ceramic Nanocomposite Assembled through Layer-by-Layer Adsorption. *Nano Lett.* **2004**, *4*, 823–825.

52. Kharlampieva, E.; Zimnitsky, D.; Gupta, M.; Bergman, K. N.; Kaplan, D. L.; Naik, R. R.; Tsukruk, V. V. Redox-Active Ultrathin Template of Silk Fibroin: Effect of Secondary Structure on Gold Nanoparticle Reduction. *Chem. Mater.* **2009**, *21*, 2696–2704.